

# Monomeric red fluorescent proteins with a large Stokes shift

Kiryl D. Piatkevich<sup>1</sup>, James Hulit<sup>1</sup>, Oksana M. Subach, Bin Wu, Arian Abdulla, Jeffrey E. Segall, and Vladislav V. Verkhusha<sup>2</sup>

Department of Anatomy and Structural Biology and Gruss-Lipper Biophotonics Center, Albert Einstein College of Medicine, 1300 Morris Park Avenue, Bronx, NY 10461

Edited\* by Jennifer Lippincott-Schwartz, National Institutes of Health, Bethesda, MD, and approved January 14, 2010 (received for review December 14, 2009)

Two-photon microscopy has advanced fluorescence imaging of cellular processes in living animals. Fluorescent proteins in the blue-green wavelength range are widely used in two-photon microscopy; however, the use of red fluorescent proteins is limited by the low power output of Ti-Sapphire lasers above 1,000 nm. To overcome this limitation we have developed two red fluorescent proteins, LSS-mKate1 and LSS-mKate2, which possess large Stokes shifts with excitation/emission maxima at 463/624 and 460/605 nm, respectively. These LSS-mKates are characterized by high pH stability, photostability, rapid chromophore maturation, and monomeric behavior. They lack absorbance in the green region, providing an additional red color to the commonly used red fluorescent proteins. Substantial overlap between the two-photon excitation spectra of the LSS-mKates and blue-green fluorophores enables multicolor imaging using a single laser. We applied this approach to a mouse xenograft model of breast cancer to intravital study the motility and Golgi-nucleus alignment of tumor cells as a function of their distance from blood vessels. Our data indicate that within 40  $\mu$ m the breast cancer cells show significant polarization towards vessels in living mice.

cell polarity | intravital imaging | Keima | two-photon microscopy | mKate

A wide diversity of fluorescent proteins (FPs) of various emission wavelengths isolated from marine organisms and improved with mutagenesis has found numerous applications in biotechnology, cell biology, medicine as probes for noninvasive labeling and tracking of proteins, organelles, and cells in real time (1). Together with the introduction of two-photon (2P) laser-scanning microscopy, FPs allow visualization in vivo of cell motility, changes in gene activity, and protein localization in intact tissues and living organisms (2, 3) due to less photodamage and less photobleaching outside of the focal plane, as well as reduced autofluorescence background compared to one-photon confocal microscopy (4, 5). The ability to perform multicolor 2P microscopy is desirable in order to allow simultaneous visualization of multiple processes in vivo simultaneously. Among FPs, red fluorescent proteins (RFPs) are of particular interest (6). The red emission spectrum has lower signal from cellular autofluorescence, and light-scattering intensity drops off as the wavelength increases, allowing greater imaging depth. Furthermore, longer wavelengths cause less damage to proteins and DNA. Hence, RFPs have great potential as labels for tissue imaging of living animals (7). Because of the expense of Ti-Sapphire lasers used in 2P imaging, most systems have a single laser, making it impossible to efficiently excite both RFPs and other FPs such as EGFP or enhanced cyan fluorescent protein (ECFP) (8, 9); in addition, current Ti-Sapphire lasers have low power output in the excitation wavelengths for RFPs (10). One approach is to shift the excitation spectrum of RFPs through generation of RFPs with large Stokes shifts. Currently, the only RFP with a large Stokes shift allowing efficient excitation with standard 2P sources is mKeima (9). The EGFP-mKeima and ECFP-mKeima combinations have been reported as suitable for dual-color 2P microscopy (11). However, several biochemical and photochemical properties of

mKeima required for the effective use as a protein tag appear to be suboptimal.

In this paper, we applied random and rational mutagenesis to monomeric far-red mKate (6) to develop two large Stokes shift RFPs, named LSS-mKate1 and LSS-mKate2. We then utilized the LSS-mKate1 variant simultaneously with ECFP and EGFP (or FITC) for multicolor intravital imaging of tumor cell migration and polarization in living mice using 2P microscopy.

## Results

**Development of Large Stokes Shift Red Proteins.** Among the available far-red fluorescent proteins, the recently developed mKate is substantially brighter than HcRed or mPlum, which have similar excitation and emission spectra. We therefore selected mKate as a promising precursor to develop large Stokes shift RFPs. We first applied several rounds of random mutagenesis to the mKate gene using an error-prone polymerase chain reaction. Bacterial libraries consisting of up to  $7 \times 10^7$  clones were subjected to screening with a fluorescence activated cell sorter (FACS) followed by selection of the appropriate clones on Petri dishes using a fluorescence stereomicroscope. After each round, the 25–30 brightest large Stokes shift clones with minimal fluorescence in other spectral regions were analyzed by sequencing. A mixture of the selected variants was then used as a template for the next round of mutagenesis. If during the screening, external mutations at the  $\beta$ -can dimerizing interfaces (12) were observed, they were reversed by site-specific mutagenesis.

After the first round, several mutants were identified which did not fluoresce when excited with the 568 nm Kr laser line but exhibited a red emission when excited with the 407 nm Kr laser line by FACS. In addition, they emitted significant green fluorescence under violet light. Compared to mKate, the mutants had various combinations of the T62T,I; T98T,S,A; S148S,D,N; S165S,G,V,D,N; and M167M,K,E,S,D,N substitutions (numbering follows an alignment with EGFP, see Fig. S1). We found that the single mutations S148D or S165D or M167K,E,D were enough for the large Stokes shift phenotype. To eliminate the green fluorescence excited by violet light and increase the red large Stokes shift brightness, we next used the mixture of the 10 best mutants to perform random mutagenesis. The libraries of mutants were sorted using the 356 nm Kr laser line with 530/40 nm emission

Author contributions: K.D.P. and O.M.S. developed proteins; K.D.P. and B.W. characterized them in vitro; K.D.P. performed subcloning; K.D.P. and J.H. characterized proteins in cells; J.H. established stable cell lines and performed studies with 2P imaging; A.A. and J.H. performed image and cell polarization analyses; J.E.S. and V.V.V. designed and planned the project; V.V.V. designed research; K.D.P., J.H., and B.W. performed research; K.D.P., J.H., O.M.S., B.W., A.A., J.E.S., and V.V.V. analyzed data; and J.E.S., V.V.V., J.H., and K.D.P. wrote the paper.

The authors declare no conflict of interest.

\*This Direct Submission article had a prearranged editor.

<sup>1</sup>K.D.P. and J.H. contributed equally to this work.

<sup>2</sup>To whom correspondence should be addressed. E-mail: vladislav.verkhusha@einstein.yu.edu.

This article contains supporting information online at [www.pnas.org/cgi/content/full/0914365107/DCSupplemental](http://www.pnas.org/cgi/content/full/0914365107/DCSupplemental).

filter as the negative selection criterion and the 457 nm Ar excitation line with 580 nm longpass emission filter for positive selection. After two sequential rounds of random mutagenesis, four large Stokes shift RFP mutants with the additional mutations P131T/M167E/T183S/M196V, T62I/T98S/P131T/S165D, T62I/P131T/S165G/M167K, or F82I/S148D/S165G/M167S, respectively, were found. These variants had red fluorescence with excitation/emission maxima at around 460/620 nm, respectively. We evaluated the brightness, photostability, and spectral properties of these mutants and chose the mKate/P131T/M167E/T183S/M196V mutant for further improvement of photostability. Using simultaneous site-specific mutagenesis we constructed a library, in which residues 69, 148, 165, and 167 were randomized. These positions were identified from the X-ray structure of mKate (13) and substitutions which were shown to affect photostability of TagRFP variants (14). Using a custom array of 36 high-power 455 nm light-emitting diodes, we photobleached 10 cm Petri dishes with bacterial colonies expressing the FP mutants and selected those which maintained the most fluorescence. As a result, the mKate/K69Y/P131T/S148G/M167E/T183S/M196V and mKate/K69Y/P131T/S148G/S165A/M167D/T183S/M196V mutants were found. We named these mutants LSS-mKate1 and LSS-mKate2, respectively (Fig. S1). The LSS-mKate1 and LSS-mKate2 variants were 2–3-fold more photostable than their precursor.

**Characterization of the Purified LSS-mKate Variants.** We further characterized the LSS-mKate1 and LSS-mKate2 purified proteins and compared their properties with those of mKeima. LSS-mKate1 and LSS-mKate2 exhibited excitation/emission peaks at 463/624 and 460/605 nm, respectively (Fig. 1A and Table 1). Both proteins did not have any additional peaks in absorbance or fluorescence spectra. In contrast, mKeima had two excitation peaks at 440 and 584 nm, with an emission peak at 620 nm. The absorbance of mKeima had the same maxima as the fluorescence excitation spectra. The external mutations in LSS-mKates were located outside of the dimerization interfaces. In seminitative polyacrylamide gels, LSS-mKates ran as a monomer

while mKeima dimerized even at a relatively low concentration of 50  $\mu\text{g/ml}$  (Fig. S2).

Molar extinction coefficients for LSS-mKate1 and LSS-mKate2 measured using the alkaline denaturation assay (15, 16) were 31,200 and 26,000  $\text{M}^{-1} \text{cm}^{-1}$ , with quantum yields at pH 7.5 of 0.08 and 0.17, respectively. Based on these measurements, the relative molecular brightness of LSS-mKate1 and LSS-mKate2 are 0.78 and 1.37 of that of mKeima (Table 1).

LSS-mKate1 and LSS-mKate2 had rapid chromophore maturation at 37  $^{\circ}\text{C}$  with maturation half-times of 100 and 150 min, respectively (Fig. 1B). In the same conditions, mKeima matured 1.8–2.6-fold more slowly with a maturation half-time of 270 min. The fluorescence of LSS-mKate1 and LSS-mKate2 was extremely pH stable with  $\text{pK}_a$  values of 3.2 and 2.7, respectively (Fig. 1C), allowing their targeting to acidic cellular compartments (Fig. S3). The fluorescence changed about 20% and 25% for LSS-mKate1 and LSS-mKate2, respectively, with pH changes in the physiological range of 5.0–8.0 (Fig. 2A and B). In contrast, mKeima had the  $\text{pK}_a$  equal to 6.0 (Fig. 1C). Moreover, with alkalization from 5.0 to 8.0 the fluorescence of mKeima increased almost 3-fold and decreased more than 12-fold when excited at 440 nm and 584 nm, respectively (Fig. 1C).

To determine photostability of LSS-mKates, we performed photobleaching experiments in aqueous drops of the purified proteins in oil using an epifluorescence microscope equipped with a 200 W metal-halide arc lamp and 436/20 or 480/40 nm filters for bleaching. The raw photobleaching data were normalized to absorbance spectra of the proteins, spectra of the arc lamp, and filter transmission. The photostability for LSS-mKate1 and LSS-mKate2 was 3.2-fold and 2.3-fold higher, respectively, than that for mKeima, and 1.9-fold and 2.6-fold lower than that for EGFP (Fig. 1D). The dimerization of mKeima may substantially increase its brightness, photostability, and rate of maturation (Table 1), as has been observed for dimeric variants of other FPs including Katushka (6) and dEosFP (17).

In order to test the applicability of LSS-mKates for 2P microscopy, we measured their action cross-sections ( $\sigma_{2\text{PE}}$ ) values and compared with those of ECFP, EGFP, and mKeima. It has been

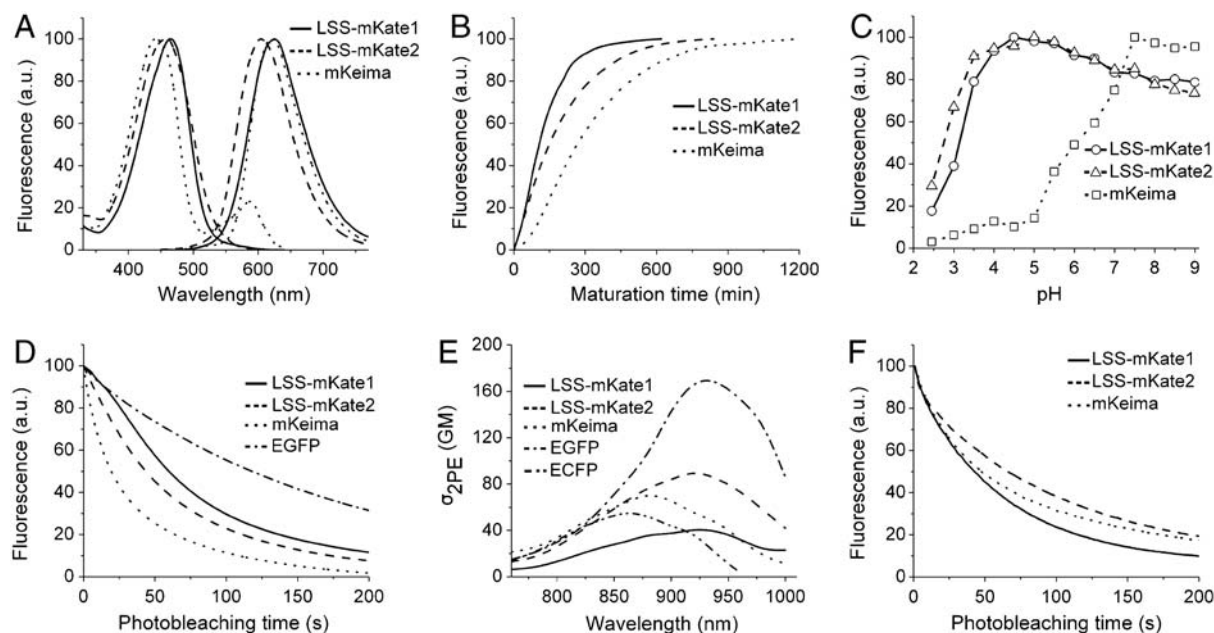


**Fig. 1.** Spectral, biochemical, and photobleaching properties of LSS-mKate1 (solid line), LSS-mKate2 (dashed line), and mKeima (dotted line). (A) Normalized fluorescence one-photon excitation and emission spectra. (B) Fluorescence maturation kinetics. (C) pH dependence of fluorescence. (D) Normalized curves of photobleaching in aqueous drops in oil using wide-field epifluorescent illumination measured for LSS-mKates, mKeima, and EGFP (dashed-dotted line). (E) Two-photon action cross-sections ( $\sigma_{2\text{PE}}$ ) measured for LSS-mKates, mKeima, EGFP, and ECFP (double-dashed-dotted line). (F) Photobleaching curves for the proteins targeted to nuclei of live HeLa cells measured using 2PE at 870 nm. Each curve represents data averaged over 16–20 cells.

**Table 1. Properties of the LSS-mKate variants in comparison with mKeima**

Protein	Excitation maximum (nm)	Emission maximum (nm)	Extinction coefficient (M <sup>-1</sup> cm <sup>-1</sup> )	Quantum yield	Relative brightness	Photostability, wide field (s)	pKa	Maturation at 37 °C (min)
LSS-mKate1	463	624	31,200	0.08	0.78	60	3.2	100
LSS-mKate2	460	605	26,000	0.17	1.37	44	2.7	150
mKeima	440	620	13,400(14,400)	0.24	1.00	19	6.0 (6.5)	270
	584	620	2,500	0.17	ND	ND	ND	ND

mKeima characteristics from the original paper (8) are shown in parentheses. Spectroscopic parameters were determined in PBS at pH 7.5. ND, not determined.

shown that  $\sigma_{2PE}$  cannot be readily predicted from one-photon absorbance spectra (10). In the range of 760–1,000 nm the  $\sigma_{2PE}$  value for LSS-mKate1 was 1.6-fold lower, and for LSS-mKate2 was 1.4-fold higher than that for mKeima (Fig. 1E). The  $\sigma_{2PE}$  maxima for both LSS-mKates were at 920 nm. There were substantial  $\sigma_{2PE}$  spectral overlaps between LSS-mKates, ECFP, and EGFP. The data suggested that LSS-mKates could be used for multicolor 2P imaging with ECFP and EGFP, or with ECFP and FITC (see FITC  $\sigma_{2PE}$  spectrum in ref. 18).

Photobleaching of LSS-mKates and mKeima under 2PE was measured with proteins targeted to the nuclei of live HeLa cells using 870 nm excitation by a Ti-Sapphire laser. The 2P photostability of LSS-mKate1 was similar to that of mKeima, and the 2P photostability of LSS-mKate2 was 1.4-fold higher than for mKeima (Fig. 1F). The difference between the one- and two-photon photostability is possibly caused by different protein environments (aqueous drops vs. nuclei). It has been shown that the FP photoconversion and photobleaching are substantially affected by endogenous oxidizers present in live cells (19).

**Behavior of the LSS-mKate Variants in Live Cells.** To characterize LSS-mKates in cells, we first performed transient transfection of HeLa cells with nontargeted LSS-mKates and imaged them either using wide-field epifluorescence or confocal microscopes. The fluorescence was evenly distributed within the cytosol and nucleus of live HeLa cells without any aggregation or nonspecific localization. We then fused LSS-mKates with  $\beta$ -actin,  $\alpha$ -actinin, paxillin, keratin,  $\alpha$ -tubulin, H2B, and cytochrome C oxidase. The fusion constructs incorporated well into endogenous structures, indicating that LSS-mKates exhibit monomeric behavior in cells (Figs. S4 and S5).

Not all fusions with mKeima, however, incorporated well into endogenous cellular structures (Fig. S6). Moreover, some fusions exhibited notable aggregation (Fig. S6 A, B, and E) and intracellular background (Fig. S6 A, C, and E). In the original paper describing mKeima (8), oligomerization studies relied upon an equilibrium sedimentation approach with a tetrameric DsRed molecular weight standard only. Later, it was shown that mKeima could be targeted to organelles such as mitochondria

(9); visualization of the tubulin cytoskeleton, however, was performed using a tandem version, tdKeima (11). Together with our *in vitro* analysis, these data suggest that mKeima has a tendency to form dimers.

LSS-mKates brightness and photostability allowed time-lapse imaging of the intracellular dynamics (Movie S1). The normalized photostabilities of LSS-mKate1 and LSS-mKate2 in live HeLa cells were 3.6-fold and 2-fold higher than that of common ECFP (Fig. S7).

Preclonal mixtures of human mammary adenocarcinoma MDA-MB-231, rat mammary adenocarcinoma MTLn3 and MTLn3 cells overexpressing ErbB1 (20) stably expressing LSS-mKates either in cytosol or targeted to the nucleus had high brightness and normal *in vitro* proliferation rates indicating low cytotoxicity. The stable cell lines exhibited good photostability during time-lapse imaging (Fig. S8 and Movies S2 and S3) with photobleaching half-times similar to those observed with the purified LSS-mKates.

To verify the utility of the LSS-mKates as an additional red color for imaging with common RFPs, fusion constructs of LSS-mKates and mKeima were coexpressed with mCherry- $\alpha$ -tubulin, TagRFP- $\alpha$ -actinin, and mKate-VSVG (vesicular stomatitis virus G protein tS045) in live HeLa cells (Fig. 3). Two sets of filters allowed visualization of both LSS-mKates with mCherry, TagRFP, or mKate without any cross-talk between the channels. mKeima exhibited a strong red fluorescence when excited with 570/30 light, however, which hindered imaging of the mCherry- $\alpha$ -tubulin, TagRFP- $\alpha$ -actinin, or mKate-VSVG structures separately from the mKeima fusions. Even at high expression levels, no red fluorescence of LSS-mKates was observed upon 570/30 nm excitation (Fig. S9).

**Intravital Imaging of LSS-mKate1 in Mice.** We next examined the use of LSS-mKates under 2PE using a xenograft mouse model by orthotopically transplanting the metastatic mammary adenocarcinoma MTLn3 or MTLn3 cells overexpressing ErbB1 (20). We stably coexpressed LSS-mKates targeted to the nucleus. To distinguish the different constructs, the LSS-mKate1 cells were cotransfected either with ECFP targeted to Golgi or both ECFP

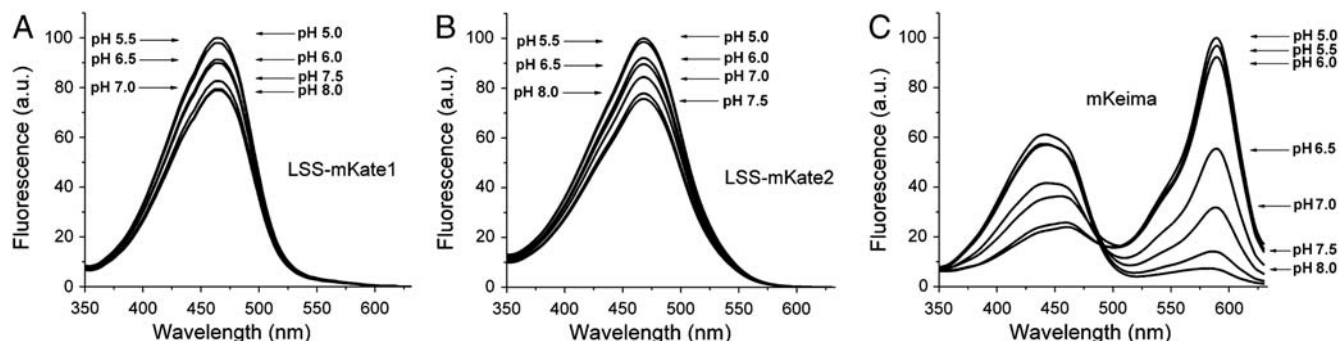


**Fig. 2.** Changes of the one-photon excitation fluorescence spectra for the purified (A) LSS-mKate1, (B) LSS-mKate2, and (C) mKeima proteins in the physiological pH range of 5.0–8.0. Emission of the protein samples was detected at 675 nm.

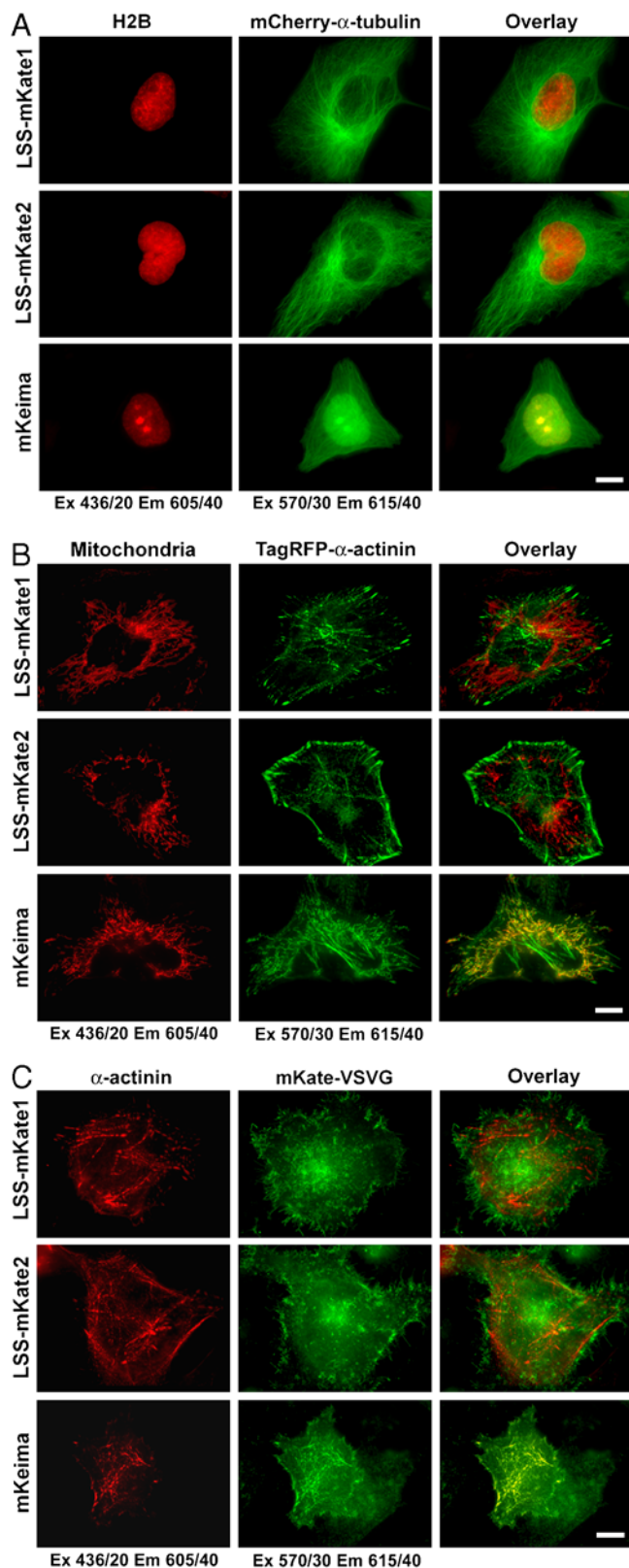


**Fig. 3.** LSS-mKate1, LSS-mKate2, and mKeima proteins fused to H2B (A), cytochrome C oxidase subunit VIII (B) or  $\alpha$ -actinin (C) were coexpressed with either mCherry- $\alpha$ -tubulin (A), TagRFP- $\alpha$ -actinin (B) or mKate-VSVG (C) in live HeLa cells. The large Stokes shift fluorescence images (left columns; red color) were acquired using 436/20 excitation and 605/40 emission filters. The standard red fluorescence images (middle columns; green pseudocolor) were acquired using 570/30 excitation and 615/40 emission filters. The right columns are the overlay of the left and center columns. Bars are 10  $\mu$ m.

targeted to Golgi and cytoplasmic EGFP. After transplantation, mammary tumors were allowed to grow over a four-week period and then were imaged. Intravital imaging was performed by making a skin flap to expose the tumor (20); 870 nm was found to be the optimal wavelength for simultaneous 2PE of LSS-mKates, ECFP, and EGFP (see [Movie S4](#)). The fluorescence of the LSS-mKates was present in all cells, indicating that the expression of this protein was tolerated by the cells. LSS-mKate2 fluorescence was about 2-fold higher than that of LSS-mKate1. We further concentrated on imaging of LSS-mKate1 tumor cells. We reasoned that if we could intravital detect LSS-mKate1 then we could reliably image LSS-mKate2, which had the higher  $\sigma_{2PE}$  and better 2P photostability.

Tumors were imaged to Z-axis depths of 60  $\mu$ m to study cell motility and 40  $\mu$ m for cell polarization analysis. 2P photostability of LSS-mKate1 allowed for imaging time intervals of long enough duration so as to capture tumor cell migration of the ErbB1-expressing cell line (Fig. 4). Tumors were imaged using an accumulation scanning mode ( $N = 2$ ) at a scanning speed of 166 lines per second, over a 45–60-min time span with Z-series scans spaced at 5-min intervals. We were able to image Golgi-nucleus pairs migrating through the tumor stroma for up to 1 h ([Movies S5–S7](#)).

The use of LSS-mKate1 in combination with ECFP allowed us to image tumor cells in living mice with a level of subcellular resolution which permitted detailed compartmental spatial identification. We took advantage of this resolution to assess *in vivo*

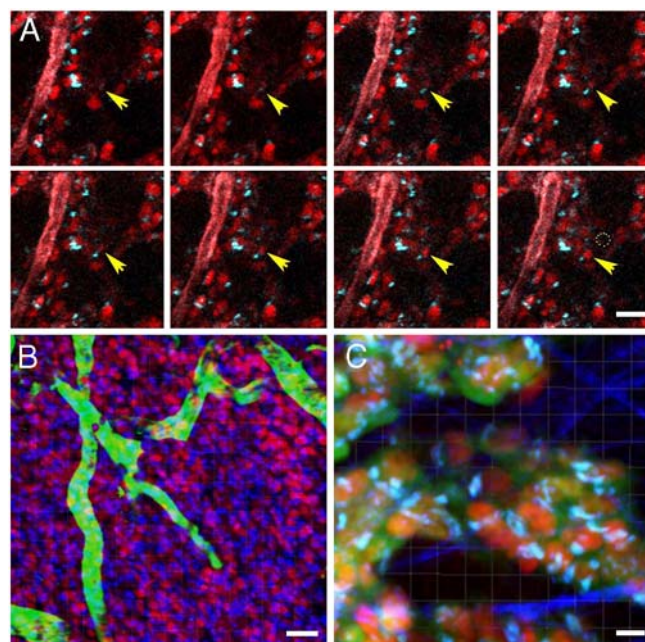


**Fig. 4.** Intravital imaging of tumor cell motility using 2PE. MTLn3 cells overexpressing ErbB1 with stable coexpression of NLS-LSS-mKate1 (nucleus, red) and GalT-ECFP (Golgi, blue) were imaged. FITC-labeled 70 kDa dextran was injected prior to the start of imaging. (A) Series of still images extracted from 40-min time-lapse sequence shows a nucleus-Golgi pair (yellow arrows) migrating into the plane and through the tumor, while the dotted circle (40-min image) indicates the original entry position of the nucleus-Golgi pair. The FITC-labeled blood vessels appear in red. (B) Three color image of NLS-LSS-mKate1 (nucleus, red), GalT-ECFP (Golgi, blue) with FITC-conjugated 70 kDa dextran (vasculature, green, injected into the tail vein). Z-series were captured at 2  $\mu$ m steps, and 3D reconstruction was processed using Imaris software. (C) MTLn3 cells stably coexpressing GalT-ECFP (Golgi, cyan), NLS-LSS-mKate1 (nucleus, red), and EGFP (cytoplasm, green) were imaged simultaneously with second-harmonic generated signal from collagen fibers (blue). Complete sets of the time-lapse images B and C are available as [Movies S5](#) and [S6](#), respectively. All images were captured using a single 870 nm wavelength 2PE and 20 $\times$  NA 0.95 objective lens. Bars are 50  $\mu$ m (A, B) and 10  $\mu$ m (C).

Golgi-nucleus alignment of potentially polarized cells (Fig. 5), as the Golgi has been reported to precede the nucleus during wound-induced migration (21) (Movie S8). In addition, we have demonstrated tumor cell polarization occurs adjacent to blood vessels (22). Therefore, we analyzed the Golgi-nucleus alignment toward tumor blood vessels as a function of their distance from the vessels (Fig. 5C). Z-axis series were captured at 2  $\mu\text{m}$  steps and Golgi angles were calculated in relation to a perpendicular orientation between the nucleus of the cell and the nearest blood vessel (Fig. 5B, diagram). Blood vessels were segmented into linear regions for the analysis (Fig. 5A, yellow dotted lines). Comparisons were made between orientations producing angles less than 90° to angles greater than 90° (Golgi preceding nucleus = 0 degrees). Although at distances greater than 40  $\mu\text{m}$  from the vessel Golgi angles were randomly distributed (0–180°), within 40  $\mu\text{m}$  there was a 50% increase in Golgi-nucleus pairs with angles less than 90° ( $P < 0.05$ ). However, within 40  $\mu\text{m}$  not all vessel segments displayed the increase in low-angle Golgi-nucleus orientations (Fig. 5D). Of the 21 segments which had Golgi-nucleus pairs within 40  $\mu\text{m}$ , roughly 70% of the segments possessed a majority of Golgi-nucleus pairs with angles less than 90°. Almost 25% of the vessel segments showed a 2-fold greater

number of Golgi-nucleus pairs with low-angle alignments, indicating a polarization towards the blood vessel.

## Discussion

The primary goal of this study was to develop monomeric large Stokes shift RFPs for multicolor 2P microscopy. Our directed molecular evolution approach has resulted in the development of the LSS-mKate1 and LSS-mKate2 variants. We have identified six amino acid mutations present in these proteins compared to parental mKate (Fig. S1). Among them K69Y, S148G, M167E,D, and T183S are internal to the  $\beta$ -can mKate fold and P131K and M196V are external to the fold.

LSS-mKates contain either M167E or M167D substitution. According to the mKate crystal structure (13), the hydroxyl group of Tyr66 in the chromophore is most proximal to residues 148 and 167. We therefore suggest that in LSS-mKates, the chromophore tyrosine hydroxyl makes hydrogen bonds with the side chain of amino acid 167. It is expected that in the ground state, the pKa of the D167/E167 carboxylates is lower than the pKa of the Y66 side chain hydroxyl, suggesting that the chromophores can be stabilized in their neutral forms. This is consistent with the excitation spectra of both LSS-mKates having maxima at  $\sim 460$  nm, which is characteristic for the neutral DsRed-like chromophore (23–25). Upon excitation of the neutral chromophore, the pKa values drop by several units (23) leading to the formation of an anionic chromophore, which subsequently emits a red photon. Therefore, we propose that the D167/E167 residues are mainly responsible for the large Stokes shifts in LSS-mKates by enabling an excited-state proton transfer (ESPT) from the chromophore tyrosine hydroxyl to the side chain of the 167 residue, as occurs in mKeima (24, 25). Notably, mKate mutants with the residue 167 substituted with Lys (a proton acceptor amino acid) found during our screening also had a large Stokes shift. In addition, the mKate/S148D and mKate/S165D mutants exhibited large Stokes shifts. A blue shift in the red fluorescence maxima of LSS-mKates comparing to mKate can be attributed to the formation of a hydrogen bond between the chromophore and Asp167/Glu167 side chains and to changes in the immediate chromophore environment.

Despite the limited brightness of LSS-mKates in comparison with common RFPs (the brightness of LSS-mKate1 and LSS-mKate2 is  $\sim 28$  and  $\sim 50\%$  of that of mKate), it is sufficient to image tagged proteins, organelles, and cells in culture and in live mice (Movie S4). Structural and spectroscopic studies of the GFP mutants exhibiting ESPT suggest that their brightness depends on the chromophore coplanarity and the efficiency of the proton transfer (26). In addition, the geometry of the hydrogen bonds plays an important role in the proton transfer. Future crystallographic analysis of LSS-mKates should help to optimize the proton transfer pathway(s) and to increase their brightness.

We imaged LSS-mKate1 intravitally using 2PE. First we sought to assess its fluorescent intensity and photostability by monitoring tumor cell movement that, based on our previous work, requires a minimum of 30 min of time-lapse imaging to capture (22). Second, by compartmentalizing the LSS-mKate1 expression we evaluated tumor cell polarity in vivo. Polarization of tumor cells is an indication of gradient sensing during chemotaxis and, we hypothesize, also a feature of invading tumor cells. Furthermore, we aimed to develop a cell line which could potentially act as a chemotactic gradient sensor to assist in characterization of the tumor microenvironment and metastatic process. Prior work by others has demonstrated that during in vitro wound closure involving either normal rat kidney, endothelial or rat embryonic cells, the Golgi complex (21, 27, 28), perhaps in close association with the microtubule-organizing center (27, 29), precedes the nucleus during directed cell migration. However, not all studies are in agreement with these findings (30), and the orientation of the Golgi with respect to the nucleus may be both cell type and

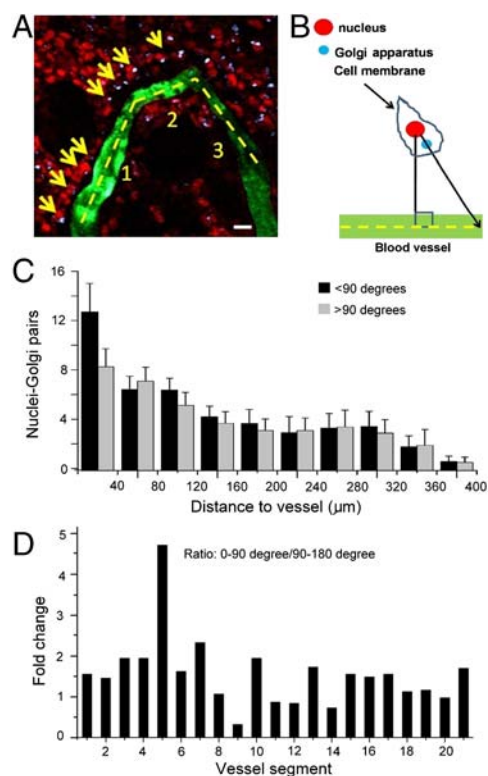


**Fig. 5.** In vivo nucleus-Golgi alignment and cell polarization imaged using 2PE. MTLn3 cells overexpressing ErbB1 with stable coexpression of NLS-LSS-mKate1 (nucleus, red), and GalT-ECFP (Golgi, blue) were imaged. FITC-labeled 70 kDa dextran was injected prior to the start of imaging. (A) Still image from 40  $\mu\text{m}$  thick Z-series shows nucleus-Golgi pairs (yellow arrows) aligned adjacent to a tumor blood vessel. Bar is 50  $\mu\text{m}$ . (B) Diagram indicating method for calculation of angle of nucleus-Golgi axis relative to perpendicular distance from vessel. Nucleus-vessel distances were calculated to linear line segments [examples shown in (A) yellow-dotted lines labeled as 1, 2 and 3]. (C) Analysis of nucleus-Golgi-vessel angles. Horizontal axis displays vessel to nucleus distances, vertical axis displays the number of nucleus-Golgi pairs displaying either a low angle (<90°, black bars) or high angle (>90°, gray bars) as calculated relative to the nearest blood vessel segment. Data are displayed as mean  $\pm$  SEM. Bar graph (D) displays the ratio of the number of low angled nucleus-Golgi pairs (<90°) to high angled nucleus-Golgi pairs (>90°) in the 0–40  $\mu\text{m}$  range for 21 different vessel segments.

microenvironment specific. The use of nuclear localized LSS-mKate1 in combination with Golgi-targeted ECFP allowed us to image tumor cells in living mice at a level of subcellular resolution which permitted detailed compartmental spatial identification. We took advantage of this resolution to calculate the in vivo Golgi-nucleus-vessel alignments of potentially polarized cells.

We previously observed that tumor cell migration and invasion in vivo occurs more frequently near blood vessels (3, 31). Therefore, we examined tumor cell Golgi-nucleus alignments as a function of blood vessel distance. As observed here during time-lapse imaging, Golgi positioning within the tumor cell was a dynamic process. Repositioning of the Golgi occurred even when the tumor cell nucleus remained stationary, perhaps suggesting Golgi repositioning might be under the control of the cells' directional sensing pathways (32). We found that beyond 40  $\mu\text{m}$  from the vessel, there is a random orientation of Golgi-nucleus-vessel angles. However, within 40  $\mu\text{m}$  more cells assume an orientation of less than 90°. These data agree with our previous observations, in which we found that tumor cell motility and polarization occurred only in limited areas of the tumor microenvironment (22), especially near blood vessels. Here we have extended those observations by determining that the polarization appears to be strongest next to the vessel and drops off rapidly with distance from the vessel, suggesting that the cues driving the polarization are local. The use of the Golgi-nucleus orientation provides a more quantitative measure of tumor cell polarization in vivo. These data also demonstrate that local tumor microenvironments can differentially influence cell invasion and migration.

## Conclusions

Compared to the only available red large Stokes shift protein mKeima, the LSS-mKate1 and LSS-mKate2 proteins have substantially higher pH stability, better photostability, faster chromophore maturation and monomeric behavior. Moreover, they lack the excitation peak at ~580 nm allowing their simultaneous imaging with common RFPs. Importantly, LSS-mKates combine both a red emission and a large Stokes shift, both necessary for 2P

imaging of live tissues. Due to substantial overlap between the 2P action cross-sections for ECFP and EGFP/FITC, LSS-mKates enable simultaneous multicolor intravital imaging using 2PE.

## Materials and Methods

The experimental procedures are briefly sketched here; a detailed description is provided as *SI Text*. Site-specific mutagenesis was performed using the QuikChange Mutagenesis Kit (Stratagene). Random mutagenesis was performed with the GeneMorph II Random Mutagenesis Kit (Stratagene). For screening of libraries of mutants a MoFlo XDP cell sorter (Beckman Coulter) equipped with standard Ar, Kr, and Ar-Kr mixed-gas lasers was used.

For spectroscopic analysis, mKeima, LSS-mKates, and various mutants were expressed and purified as described previously (6). Absorbance spectra were recorded on a U-3010 spectrophotometer (Hitachi). Excitation and emission spectra were measured using a FluoroMax-3 spectrofluorometer (Jobin Yvon).

Measurement of 2P action cross-sections was performed as described previously (33) using a Cameleon Ultra Ti-Sapphire laser system (Coherent). 2P photobleaching was conducted at 870 nm with FPs expressed in nuclei of HeLa cells.

Time-lapse imaging in vitro was performed using a SP5 AOBs confocal microscope (Leica). Orthotopic injection in mammary glands of SCID mice was as previously described (20). 2P microscopy and intravital imaging procedure were performed as described previously (5). The primary tumor was surgically exposed as described (31). Tumor cell polarization analysis was performed at 870 nm; and Z-stacks were captured at 2  $\mu\text{m}$  steps over a Z-axis distance of 40  $\mu\text{m}$ . Stacks were reconstructed in ImageJ and analyzed using the Region of Interest Tracker plug-in. Nucleus-Golgi pairs within each cell were "tracked" to establish their positions (i.e. identify their x, y, z coordinates within 3D sections) and later calculate their orientations.

**ACKNOWLEDGMENTS.** We thank A. Miyawaki for mKeima, E. Snapp for GalT-ECFP, M. Davidson for  $\alpha$ -actinin, H2B, keratin, paxillin, cytochrome C oxidase subunit VIII, and R. Singer for NLS encoding plasmids. We also thank D. Entenberg and J. Condeelis for providing the ROI Tracker plug-in, R. Eddy and V. DesMarais for discussions regarding Golgi-nucleus orientation in MTLn3 cells, and J. Wyckoff, D. Kedrin, and T. Smirnova for help with in vivo imaging. This work was supported by the National Institutes of Health, Grant GM073913 (to V.V.V.) and Grants CA100324 and CA77522 (to J.E.S.).

- Stepanenko OV, et al. (2008) Fluorescent proteins as biomarkers and biosensors: Throwing color lights on molecular and cellular processes. *Curr Protein Pept Sci* 9:338–369.
- Hoffman RM (2009) Imaging cancer dynamics in vivo at the tumor and cellular level with fluorescent proteins. *Clin Exp Metastasis* 26:345–355.
- Wyckoff JB, et al. (2007) Direct visualization of macrophage-assisted tumor cell intravasation in mammary tumors. *Cancer Res* 67:2649–2656.
- Rubart M (2004) Two-photon microscopy of cells and tissue. *Circ Res* 95:1154–1166.
- Wang W, et al. (2002) Single cell behavior in metastatic primary mammary tumors correlated with gene expression patterns revealed by molecular profiling. *Cancer Res* 62:6278–6288.
- Shcherbo D, et al. (2007) Bright far-red fluorescent protein for whole-body imaging. *Nat Methods* 4:741–746.
- König K (2000) Multiphoton microscopy in life sciences. *J Microsc* 200:83–104.
- Kogure T, et al. (2006) A fluorescent variant of a protein from the stony coral *Montipora* facilitates dual-color single-laser fluorescence cross-correlation spectroscopy. *Nat Biotechnol* 24:577–581.
- Kawano H, et al. (2008) Two-photon dual-color imaging using fluorescent proteins. *Nat Methods* 5:373–374.
- Drobizhev M, et al. (2009) Absolute two-photon absorption spectra and two-photon brightness of orange and red fluorescent proteins. *J Phys Chem B* 113:855–859.
- Kogure T, Kawano H, Abe Y, Miyawaki A (2008) Fluorescence imaging using a fluorescent protein with a large Stokes shift. *Methods* 45:223–226.
- Merzlyak EM, et al. (2007) Bright monomeric red fluorescent protein with an extended fluorescence lifetime. *Nat Methods* 4:555–557.
- Pletnev S, et al. (2008) A crystallographic study of bright far-red fluorescent protein mKate reveals pH-induced cis-trans isomerization of the chromophore. *J Biol Chem* 283:28980–28987.
- Shaner NC, et al. (2008) Improving the photostability of bright monomeric orange and red fluorescent proteins. *Nat Methods* 5:545–551.
- Gross LA, et al. (2000) The structure of the chromophore within DsRed, a red fluorescent protein from coral. *Proc Natl Acad Sci USA* 97:11990–11995.
- Ward WW (2005) *Green Fluorescent Protein: Properties, Applications and Protocols*, eds M Chalfie and SR Kain (Wiley, Hoboken, NJ), pp 39–65.
- Subach FV, et al. (2009) Photoactivatable mCherry for high-resolution two-color fluorescence microscopy. *Nat Methods* 6:153–159.
- Makarov NS, Drobizhev M, Rebane A (2008) Two-photon absorption standards in the 550–1600 nm excitation wavelength range. *Opt Express* 16:4029–4047.
- Bogdanov A, et al. (2009) Green fluorescent proteins are light-induced electron donors. *Nat Chem Biol* 5:459–461.
- Xue C, et al. (2006) Epidermal growth factor receptor overexpression results in increased tumor cell motility in vivo coordinately with enhanced intravasation and metastasis. *Cancer Res* 66:192–197.
- Nobes CD, Hall A (1999) Rho GTPases control polarity, protrusion, and adhesion during cell movement. *J Cell Biol* 144:1235–1244.
- Wyckoff JB, Jones JG, Condeelis JS, Segall JE (2000) A critical step in metastasis: In vivo analysis of intravasation at the primary tumor. *Cancer Res* 60:2504–2511.
- Wiehler J, Jung G, Seebacher C, Zumbusch A, Steipe B (2003) Mutagenic stabilization of the photocycle intermediate of green fluorescent protein (GFP). *Chembiochem* 4:1164–1171.
- Violot S, Carpentier P, Blanchoin L, Bourgeois D (2009) Reverse pH-dependence of chromophore protonation explains the large Stokes shift of the red fluorescent protein mKeima. *J Am Chem Soc* 131:10356–10357.
- Henderson JN, et al. (2009) Excited state proton transfer in the red fluorescent protein mKeima. *J Am Chem Soc* 131:13212–13213.
- Shu X, et al. (2007) Ultrafast excited-state dynamics in the green fluorescent protein variant S65T/H148D. 1. Mutagenesis and structural studies. *Biochemistry* 46:12005–12013.
- Kupfer A, Louvard D, Singer SJ (1982) Polarization of the Golgi apparatus and the microtubule-organizing center in cultured fibroblasts at the edge of an experimental wound. *Proc Natl Acad Sci USA* 79:2603–2607.
- Bershady AD, Futerman AH (1994) Disruption of the Golgi apparatus by brefeldin A blocks cell polarization and inhibits directed cell migration. *Proc Natl Acad Sci USA* 91:5686–5689.
- Gotlieb AI, Spector W (1981) Migration into an in vitro experimental wound: A comparison of porcine aortic endothelial and smooth muscle cells and the effect of culture irradiation. *Am J Pathol* 103:271–282.
- Pouthis F, et al. (2008) In migrating cells, the Golgi complex and the position of the centrosome depend on geometrical constraints of the substratum. *J Cell Sci* 121:2406–2414.
- Kedrin D, et al. (2008) Intravital imaging of metastatic behavior through a mammary imaging window. *Nat Methods* 5:1019–1021.
- Devreotes P, Janetopoulos C (2003) Eukaryotic chemotaxis: Distinctions between directional sensing and polarization. *J Biol Chem* 278:20445–20448.
- Hillesheim LN, Chen Y, Müller JD (2006) Dual-color photon counting histogram analysis of mRFP1 and EGFP in living cells. *Biophys J* 91:4273–4284.